ADVANCED MATERIALS TECHNOLOGIES
www.advmattechnol.de

Roll-to-Roll Fabrication of Bijels via Solvent Transfer Induced Phase Separation (R2R-STrIPS)

*Henrik Siegel, Mariska de Ruiter, Georgios Athanasiou, Cos M. Hesseling, and Martin F. Haase**

Bicontinuous interfacially jammed emulsion gels (bijels) are soft materials with applications in separation science, energy storage, catalysis, and tissue engineering. Bijels are formed by arresting the liquid–liquid phase separation of two immiscible liquids via interfacial jamming of colloidal particles. Current fabrication methods of bijels employ either batch processing or continuous-flow microfluidic synthesis. Production methods with higher throughput are needed to facilitate large-scale synthesis of bijels. Herein, it is shown that roll-to-roll processing (R2R) enables the fabrication of bijel films with controlled dimensions at rates of several cm^3 per minute. Increasing the bijel production rate via R2R requires an understanding of the interaction of the bijel with the R2R substrate. The study demonstrates that controlling the wetting on the R2R substrate enables the synthesis of uniform bijel films with adjustable thickness. Moreover, this research shows that the bijel film microstructure depends on the mechanism of phase separation and particle surface functionalization. The resulting knowledge gains can help to leverage bijel synthesis from laboratory to industrial scales in the future, promoting the exciting application potentials of bijels.

1. Introduction

Separation membranes are porous materials used for filtration with applications in water treatment and chemical purifications.[1–3] Such semipermeable separation membranes are commonly fabricated via nonsolvent-induced phase separation (NIPS).[4] In 2015, porous materials with remarkably similar structures as NIPS membranes were obtained via a different method entitled solvent transfer induced phase separation (STrIPS).[5] During STrIPS, the porous structure is generated with a mixture of a low molecular weight oil, water, a solvent, and surface-active nanoparticles.[5] In contrast to NIPS, this porous structure is not obtained via polymer solidification,[6] but instead via the interfacial jamming of surface-active nanoparticles.[7] STrIPS yields kinetically arrested bicontinuous oil/water networks,[8] a structure defined as a bicontinuous interfacially jammed emulsion gel (bijel).[9–12] STrIPS-bijels have been employed as ultrafiltration membranes with antifouling surface coatings,[13,14] catalytic membranes,[15] liquid–liquid extraction devices[8] and as organic solvent-resistant porous materials.[16,17] Moreover, their bicontinuous structure has been shown to provide high solar reflectivity for passive cooling coatings.[18]

These promising application potentials call for scalable fabrication methods for STrIPS-bijels. While porous membranes formed via NIPS can be manufactured at industrial scales, methods to fabricate STrIPS-bijels have yielded only small laboratory quantities. Currently, STrIPS-bijels can be continuously made at rates of milliliters per hour via microfluidics.[14,15,19,20] Additionally, potentially scalable batch fabrication methods have been employed to generate bijels via other methods than STrIPS.[18,21–24] As opposed to bijel production, the mass production of flat-sheet NIPS membranes can be readily accomplished via doctor blade-, roll-, and slot die-coating.[25] Flat-sheet NIPS membrane production via these methods is straightforward due to the high viscosity (≈0.4–10 Pa s) of the NIPS precursor solution.[26,27] The viscous polymer solution facilitates the solidification via NIPS before surface tension and wetting cause deformations that impact the uniformity of the flat-sheet membrane.[6] In contrast, STrIPS precursor mixtures have viscosities of $\approx 10^{-3}$ Pa s. Thus, surface tension and (de)wetting-driven shape deformations become more challenging to control.

Here, we introduce the synthesis of flat-sheet bijels with controllable pore structures at rates of several milliliters per minute by combining STrIPS with a roll-to-roll coating (R2R-STrIPS). R2R fabrication is already extensively used for the fabrication of solar cells,[28,29] electrodes,[30] medical devices[31] and membranes.[32] To our best knowledge, the use of R2R for bijel formation has not yet been conceived. We show that despite

H. Siegel, M. de Ruiter, G. Athanasiou, C. M. Hesseling, M. F. Haase
Van't Hoff Laboratory of Physical and Colloid Chemistry
Department of Chemistry
Debye Institute for Nanomaterials Science
Utrecht University
Utrecht 3584 CH, The Netherlands
E-mail: m.f.haase@uu.nl

The ORCID identification number(s) for the author(s) of this article can be found under https://doi.org/10.1002/admt.202301525

DOI: 10.1002/admt.202301525

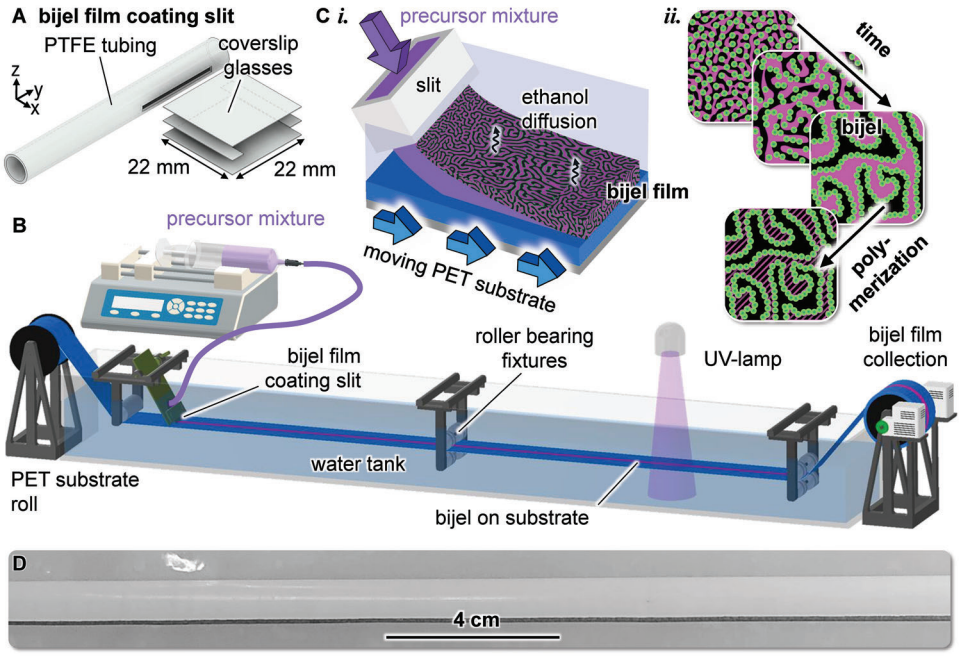

Figure 1. Continuous flow bijel film coating. A) Schematic assembly of film coating slit. B) Computer drawing of the roll-to-roll bijel film coating machine. C-*i)*. Illustration of bijel film coating on the PET substrate. *ii)*. Cartoon of bijel formation via liquid-liquid phase separation and interfacial jamming. Black color represents water, magenta color BDA, and green color Ludox TMA nanoparticles. D) Photograph of the STrIPS-bijel film (white) on PET substrate (transparent).

the low viscosity of the bijel precursor mixture, a uniform bijel film can be obtained by employing a 100 µm thin slit for the R2R-STrIPS coating. This approach renders R2R synthesis of bijels suitable for large scale bijel production. We investigate the physicochemical and engineering parameters affecting the properties of bijel films formed during R2R-STrIPS. Our research shows that bijel film formation requires the control over the wetting properties of the STrIPS precursor mixture on the R2R substrate. Moreover, control over the bijel film thickness can be attained via the R2R substrate speed and precursor mixture flow rate. Last, we analyze the structure formation of the STrIPS bijels formed via R2R and connect our findings to the mechanisms of phase separation and nanoparticle self-assembly.

2. Results and Discussion

2.1. Basics of R2R-STrIPS

Bijel film production begins by crafting a film-coating slit with microscope coverslip glasses (**Figure** 1A). We fabricate the slit of ≈100 µm height and 0.5–1.5 cm width by gluing two microscope coverslip pieces as spacers between two glass plates (see Section S1, Supporting Information). Next, the glass slit is connected to PTFE tubing and sealed with epoxy glue. This slit/tubing assembly enables the mass production of bijel films at rates of several milliliters per minute in the bijel film coating machine depicted in Figure 1B.

Bijel film coating is realized in a water-filled tank of 1–2 meters in length (Figure 1B). A long strip of polyethylene terephthalate (PET) foil (4 cm width) is submerged in water and held in place via roller-bearing fixtures. The PET foil is rolled up before and after the water tank to enable continuous R2R-STrIPS coating. We place the bijel film coating slit at an angle of ≈55° above the PET substrate by means of a 3D-printed adapter (see Section S2, Supporting Information). The slit is connected via tubing to a syringe that holds the bijel precursor mixture. This bijel precursor mixture is made of a colloidal dispersion of Ludox TMA silica nanoparticles (SNPs) in a homogeneous solution of 1,4-butanediol diacrylate (BDA), water, ethanol (EtOH), 2-hydroxy-2-methylpropriophenone (HMPP), and hexadecyltrimethylammonium bromide (CTA^+). We flow the precursor mixture via the slit onto the PET substrate using a syringe pump. At the same time, an electric motor pulls the PET substrate at a defined speed through the water tank.

As the precursor flows onto the moving PET substrate, ethanol diffuses into the surrounding water and triggers phase separation of BDA and water (Figure 1C-i, solvent transfer induced phase separation, abbreviated as STrIPS). Simultaneously, CTA^+ adsorbs on the SNPs and renders them interfacially active.[5,33,34] As a result, the CTA^+-modified SNPs stabilize the phase separating BDA/water domains via interfacial jamming (Figure 1C-ii).[14] STrIPS results in films composed of particle stabilized bicontinuous emulsion gels (bijels) with toothpaste-like consistency.

The rigidity of the bijel films can be further increased upon polymerization of BDA. To this end, a beam of UV-light is focused on the translating bijel film (Figure 1B). UV-light triggers the formation of HMPP radicals, which initiate the polymerization of the BDA and result in mechanically robust polymer/nanoparticle composite films. The solidified bijel is rolled up on the collection roll. After evaporation of water, a film with ≈1 cm width is obtained (Figure 1D) and can be detached from

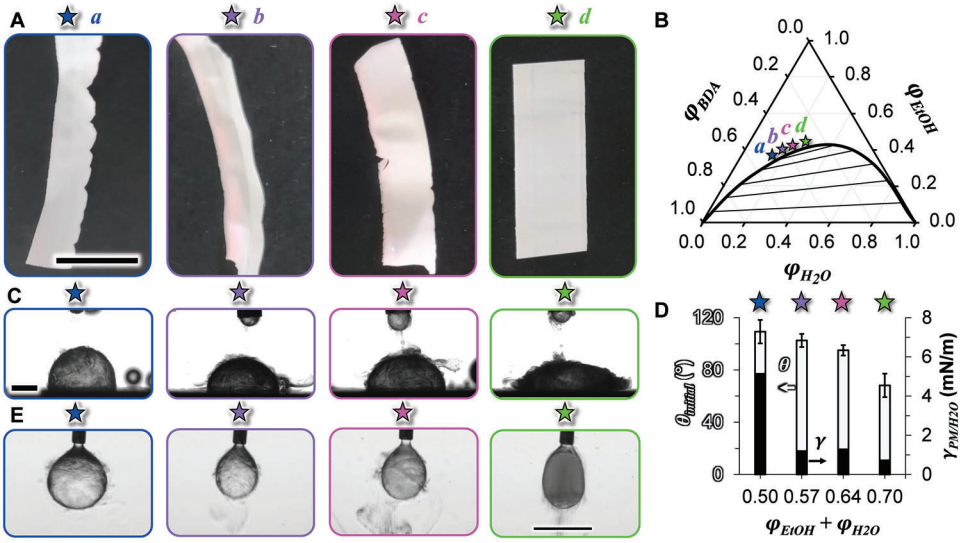

Figure 2. Macroscopic film morphology control. A) Photographs of polymerized bijel films made with precursor compositions *a–d* (scale bar is 1 cm). B) Ternary phase diagram with a binodal curve ([14]), tie-lines, and liquid compositions of precursor mixtures *a–d*. C) Photographs of precursor droplets (excluding Ludox TMA) directly after deposition on PET substrate (scale bar is 1 mm). D) Initial three-phase contact angle (θ_{initial}) of precursor droplets on PET substrate. On the secondary axis, interfacial tension of precursor mixture and water ($\gamma_{PM/H2O}$) for liquid compositions *a–d*. E) Photographs of pendant droplets of precursor mixtures *a–d* in water (excluding Ludox TMA; scale bar is 2 mm).

the PET substrate. In principle, wider films can also be fabricated via the same method by using a wider slit and coating machine. Here, the film production rate exceeds 5 cm per second, resulting in several milliliters of bijel volume per minute.

2.2. Film Uniformity Control via Wetting

The bijel film uniformity depends on the initial liquid composition of the precursor mixture. **Figure 2A** shows photographs of UV-polymerized bijel films after detachment from the substrate. From left to right we vary the initial liquid composition *a* to *d* of the precursor mixture. The corresponding volume fractions of BDA (φ_{BDA}), water (φ_{H2O}), and ethanol (φ_{EtOH}) are given in the ternary phase diagram of Figure 2B. Remarkably, flat films are obtained with composition *d*, while crumpled films with corrugated edges result from compositions *a–c*. We observe that the morphology of these films is generated while the bijel film still contains liquid BDA and while it is still attached to the PET substrate. Once UV-polymerization solidifies the film within milliseconds,[14] the highly cross-linked and rigid polyBDA does not allow for further crumbling and edge corrugations.

The trend in film morphology correlates with the wetting of the precursor mixture on the PET substrate. We demonstrate this correlation by preparing solutions of compositions *a* to *d* including 50 mM CTA^+ but excluding the silica nanoparticles. Then, a 5 µL droplet of the particle-free precursor mixture is rapidly deposited on the PET substrate submerged in water (see Video S1, Supporting Information). Figure 2C shows photographs of the moment when the droplet makes contact with the PET substrate. Once the precursor droplet is deposited, microscopic BDA droplets form by nucleation in water, resulting in light scattering around the sessile droplet. Despite this partially obstructed view, we estimate the initial contact angles (θ_{initial}) and plot the results in Figure 2D against $\varphi_{H2O} + \varphi_{EtOH}$.

$\theta_{initial}$ decreases from ≈110° to 70° as the precursor composition changes from *a* to *d*. This trend can be interpreted by considering the spreading coefficient $S = \gamma_{H_2O/PET} - \gamma_{PM/PET} - \gamma_{PM/H_2O}$, with the interfacial tensions $\gamma_{H_2O/PET}$ (water and PET-substrate), $\gamma_{PM/PET}$ (precursor mixture and PET substrate), and γ_{PM/H_2O} (precursor mixture and water). The decreasing θ_{initial} indicates enhanced spreading, signifying an increasing value of *S* from composition *a* to *d*. We measure γ_{PM/H_2O} for compositions *a*, *b*, *c*, and *d* by fitting the shape of a pendant drop of the precursor mixture in water (Figure 2E) with the Young-Laplace equation. The secondary axis in Figure 2D shows that γ_{PM/H_2O} decreases from 5.1 to 0.7 mN m^{-1} from compositions *a* to *d*. The decrease of γ_{PM/H_2O} can lead to an increase of *S*, if $\gamma_{H_2O/PET} - \gamma_{PM/PET}$ does not decrease more than γ_{PM/H_2O} decreases. Here, $\gamma_{H_2O/PET} - \gamma_{PM/PET}$ changes in dependence of $\gamma_{PM/PET}$, since $\gamma_{H_2O/PET}$ is independent of the precursor mixture compositions. We only speculate about the change of $\gamma_{PM/PET}$ from composition *a–d*. From composition *a–d*, φ_{EtOH} increases from 0.37 to 0.40, φ_{BDA} decreases from 0.43 to 0.4, and φ_{H2O} increases from 0.03 to 0.05. The increase of φ_{EtOH} can decrease $\gamma_{PM/PET}$, since the adsorption of ethanol on hydrophobic surfaces (such as PET) increases with increasing φ_{EtOH} (see molecular dynamics simulations in[35]). However, the decrease of φ_{BDA} and the increase of φ_{H2O} may have the opposite effect and increase $\gamma_{PM/PET}$. Overall, we conclude that the interfacial forces favoring spreading are dominant, since the decreasing θ_{initial} indicates an increasing value for *S* for compositions *a–d*.

The enhanced spreading of the precursor mixture on the PET substrate may explain the differences in film morphology observed in Figure 2A. After the low viscosity precursor mixture (≈10^{-3} Pa s) flows out of the rectangular coating slit, interfacial forces attempt to reshape the film into a sessile droplet with a finite contact angle. Simultaneously, the precursor mixture

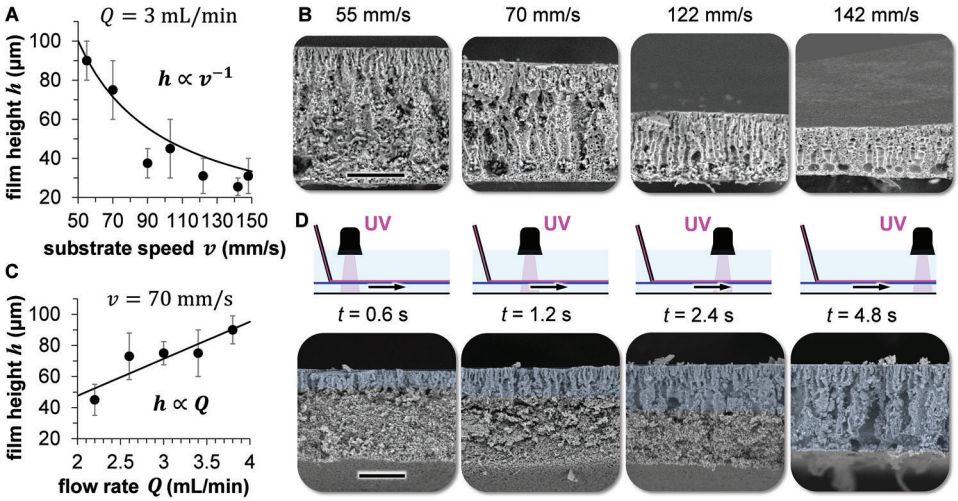

Figure 3. Film thickness and formation dynamics. A) Scanning electron microscopy images showing cross-sections of polymerized bijel films formed at different substrate speeds (scale bar is 30 µm). B) Measured (points) and calculated (lines) film thickness of bijels formed at variable substrate speed (3 mL min^{-1} precursor flow rate). Scale bars are 25 µm. C) Measured and calculated film thickness formed at variable precursor flow rates (70 mm s^{-1} substrate speed). Error bars give the standard deviation from measuring the thickness of five different membrane cross-sections. D) Scanning electron microscopy images of bijel films UV-polymerized after different substrate traveling times t (reported in seconds). The blue layer marks the progression of the bijel growth into the film over time. Scale bars are 25 µm.

solidifies as a result of interfacial particle jamming during STrIPS. We hypothesize that the competition between both processes determines the ultimate shape of the film. With high contact angles (precursor composition *a–c*), crumbling and corrugated edges are observed, because interfacial forces are strong enough for deformation before STrIPS arrests the film shape. In contrast, the interfacial forces for shape deformation are reduced for the low contact angle of precursor composition *d*. Here, rigidification preserves the initial rectangular shape of the film. Nevertheless, to fully confirm this explanation, additional experimental or computational research is needed.

Interestingly, with time, the contact angles θ of all sessile droplets *a–d* decrease and complete spreading is attained. This can occur due to the transformation of the sessile droplets into pure BDA due to the diffusion of ethanol and phase separation of water (Figure S5, Supporting Information). But, for the morphology of the bijel films in Figure 2A likely only the values for $\theta_{initial}$ are essential, since films coated with Ludox TMA particle doped precursor mixtures (pH 3) rapidly solidify due to interfacial jamming, preserving the shapes of the films.

2.3. Bijel Film Thickness Control and Structure Formation Dynamics

With the control over the precursor mixture wettability, we next investigate the bijel film height control. The graph in **Figure 3A** and the scanning electron microscope (SEM) images in Figure 3B demonstrate a decreasing film height h from 90 to 30 µm for an increasing substrate speed v from 55 to 148 mm s^{-1} at a constant precursor mixture flow rate Q = 3 mL mi^{-1} n. Alternatively, Figure 3C shows that h can also be lowered from 90 to 40 µm by decreasing Q from 3.8 to 2.2 mL min^{-1} at constant v = 70 mm s^{-1}. These trends can be rationalized with the relationship $Q = v \cdot h \cdot x$, with x the width of the films (here x = 1 cm). Figures 3A,C also contain plots of the function $h = Q \cdot x^{-1} \cdot v^{-1}$, showing that both experimental datasets are well approximated by the relation.

In situ UV-polymerization reveals the growth dynamics of the film. Figure 3D shows SEM images of films that have been exposed to UV light after different substrate traveling distances. The UV light exposure instantly polymerizes the BDA and arrests the intermediate film structure. At 0.6 s only the upper surface of the film generates pores. Over the course of 5 s, the pores grow over the full height of the film with a characteristic pore size gradient. These dynamics can be related to the diffusion of ethanol from the film to water, as was previously investigated for fibers formed via STrIPS.[14] For the bijel films, the smaller surface pores originate from the fast uptake of ethanol by the surrounding water, resulting in a rapid stabilization of the STrIPS process by the particles. The prolonged ethanol diffusion from the bottom of the film delays the arrest of the phase separation deeper inside the film resulting in a vertical coarsening of the pores. Additional insights into the formation mechanisms can be attained by varying the precursor mixture composition and analyzing the resulting structures in the following.

2.4. Bijel Structure Formation Mechanisms

Next to its effect on wettability, the precursor mixture composition also influences the mechanisms of bijel formation via STrIPS. We employ confocal laser scanning microscopy (CLSM) to analyze the structure of the polymerized bijel films. To this end, we fluorescently label polyBDA with Nile red and the SNPs with Rhodamine 110. In our CLSM images, we color the polyBDA in magenta, SNPs in green, and water in black. **Figure** 4A shows three-dimensional CLSM images of

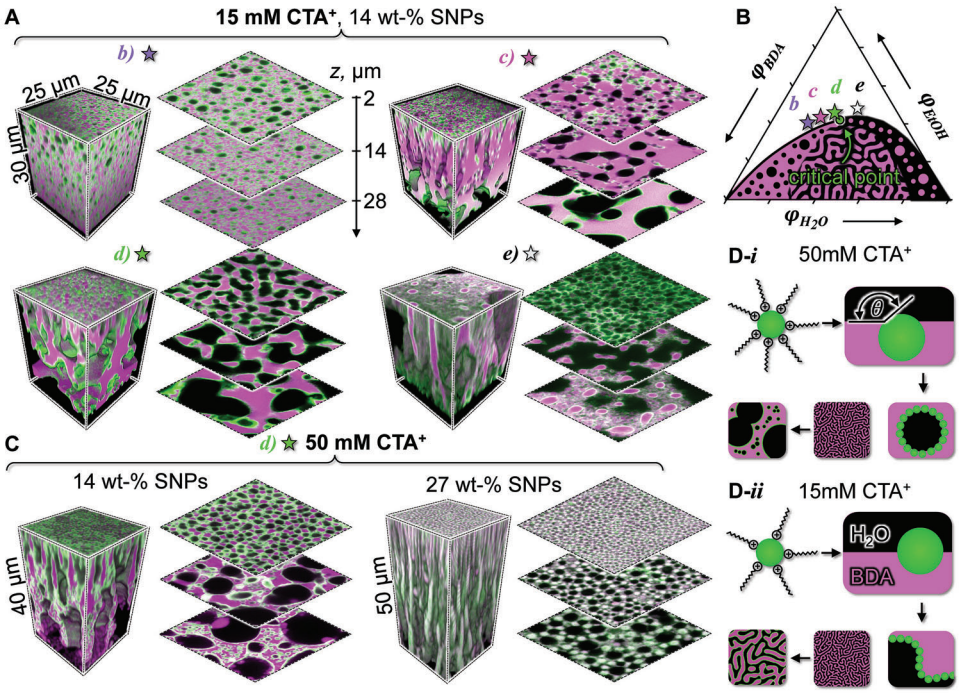

Figure 4. STrIPS-bijel film structure control. A) 3D and 2D CLSM images of bijel films made with precursor compositions *b*–*e*. The 3D images are reconstructed from CLSM *z*-stacks, and selected 2D-CLSM images from the *z*-stacks are shown at the side. B) Ternary phase diagram with schematic depictions of nucleation and spinodal phase separation. The bijel precursor compositions are labeled as *b*–*e*. C CLSM images of bijel films made with precursor composition *d* at 50 mM CTA^+ with 14 wt.% SNPs and 27 wt.% SNPs. D) Schematic depiction of CTA^+ concentration dependent functionalization of SNPs and the effects on interfacial curvature.

polymerized bijel films prepared with precursor mixtures *b* to *e* (see also Video S2, Supporting Information).

Changing the precursor compositions from *b* to *e* influences the type of phase separation during film formation. For composition *b*, spherical water droplets are surrounded by a mixed matrix of polyBDA and SNPs. With composition *c*, the water droplets extend in z-direction and form tubular pores from the upper film surface to the bottom. In contrast, for composition *d*, the polyBDA and water domains generate an interwoven network with SNPs at the interface.[36] Last, composition *e* consists of tubular polyBDA domains with vertical alignment. These different structures can be understood by inspecting the ternary phase diagram in Figure 4B.

Compositions *b* and *c* are on the left side of the critical point in the phase diagram. Thus, phase separation likely occurred via nucleation and growth of water droplets in the BDA-rich phase. In contrast, the proximity of composition *d* to the critical point suggests that the interwoven structure has formed via spinodal decomposition. Moreover, composition *e* is located on the right of the critical point, resulting in nucleation and growth of BDA droplets in a water-rich phase. When moving further right with the precursor composition than *e*, R2R-STrIPS generates fragmented structures due to the lack of a connected polyBDA scaffold. These observations demonstrate how the film structure can be manipulated via the mechanism of phase separation.

Control over the film architecture can additionally be attained via the surface functionalization of the SNPs with CTA^+. Figure 4C shows that at a concentration of 50 mM CTA^+, composition *d* generates tubular water domains with vertical alignment, similar to composition *c* at 15 mM CTA^+ in Figure 4A. This is unexpected since it was observed that composition *d* generates an interwoven BDA/water network via spinodal decomposition at 15 mM CTA^+ (Figure 4A). A possible explanation is provided in the schematic of Figure 4D-i. At 50 mM CTA^+, more CTA^+ adsorbs on the SNPs, increasing the particle hydrophobicity. More hydrophobicity can result in contact angles $\theta > 90°$.[37] SNPs with $\theta > 90°$ curve the BDA/water interface toward the water.[38,39] Thus, we speculate that the hydrophobic SNPs convert the bicontinuous fluid networks formed during the spinodal decomposition of composition *d* to tubular water domains. In contrast, we interpret that at 15 mM CTA^+ for composition *d*, the particles have $\theta = 90°$. SNPs with $\theta = 90°$ do not impose a curvature to the BDA/water interface, thereby enabling a stable bicontinuous arrangement of BDA and water as schematically depicted in Figure 4D-ii.

The bottom confocal microscopy slice in Figure 4C at 14 wt.% SNPs also show smaller discrete water droplets embedded in the polyBDA matrix. These droplets are likely a product of secondary phase separation via nucleation and growth during STrIPS.[14,40] They are stabilized by SNPs, as visible by the green fluorescence at the interface. It is likely that the high CTA^+ concentration triggers the partitioning of the SNPs into the BDA-rich phase, allowing the stabilization of the nucleated droplets.

By increasing the particle concentration to 27 wt.% at 50 mM CTA^+ in Figure 4C, the pore sizes in the film decrease. Additionally, the tubular water droplets extend deeper into the bijel film. The higher particle concentration likely enhances the stabilization of the phase separation further below the surface.

Interestingly, the circular cross sections of the tubular water domains suggest that the particles are hydrophobic for 27 wt.% particles. One might expect that an increase of the particle concentration at a constant CTA^+ concentration results in less hydrophobic particles due to a shift of the adsorption equilibrium toward lower adsorbed CTA^+ amounts. But, since the increase of the particle concentration (14–27 wt.%) is smaller than the increase of the CTA^+ concentration (15–50 mM), the adsorption equilibrium may not have shifted significantly. The high CTA^+ concentration of 50 mM may provide an excess CTA^+ amount in equilibrium with a saturated CTA^+ adsorption layer on the SNPs. The resulting anisotropic porous structures make STrIPS-bijel films an interesting nanocomposite material for applications as separation membranes.

3. Conclusion

In conclusion, this manuscript introduces a scalable method for the fabrication of bijel films in a continuous roll-to-roll-process via solvent transfer induced phase separation (R2R-STrIPS). R2R-STrIPS is realized by flowing the bijel precursor mixture through a narrow slit onto a translating plastic film in a bulk water phase. Macroscopically uniform bijel films require sufficient spreading of the bijel precursor mixture on the plastic substrate. Spreading can be achieved by changing the liquid composition of the bijel precursor mixture to decrease the interfacial tension with the bulk water phase. The thickness of the resulting bijel films can be adjusted from 30 µm to 100 µm via the bijel precursor mixture flow rate and the plastic substrate speed. Last, the bijel microstructure depends on the type of phase separation and the functionalization of the SNPs with CTA^+. Phase separation via nucleation and growth yields films with interspersed water droplets while spinodal decomposition can result in bicontinuous oil/water arrangements within the film. However, if the CTA^+ functionalization yields hydrophobic SNPs, spinodal decomposition generates elongated oil/water pores within the film. R2R-STrIPS enables the fabrication of flat-sheet bijels and nanocomposite polymer membranes at rates of cm^3 per minute; a 100–1000 times increased production rate when compared to previously reported microfluidic bijel synthesis via STrIPS. The herein-reported control over the bijel film macro- and microstructure renders industrial bijel synthesis feasible. Thus, R2R-STrIPS strongly promotes the application potentials of bijels as separation/catalytic membranes,[10,14,15] energy storage materials,[41–44] tissue engineering scaffolds,[45] and passive radiative cooling coatings.[18]

4. Experimental Section

Bijel Precursor Preparation: The bijel precursor mixture consists of Ludox TMA nanoparticles (spherical, particle diameter 20 nm; Grace) dispersed in a homogeneous mixture of 1,4-butanediol diacrylate (BDA), water, and ethanol (EtOH). The nanoparticle dispersion was prepared by concentrating 50 mL Ludox TMA from 34 to 40 wt.% by the evaporation of water (Rotary evaporator, Heidolph Instruments) at 60 °C and 140 mbar. The concentrate was centrifuged at 3270 rcf for 10 min (Allegra X-12R, Beckman Coulter) to remove particle aggregates and adjusted to pH 3 by the addition of 1 M HCl (Acros Organics).

The preparation of the precursor mixtures *b–e* was started by mixing the pure liquids BDA, water (MilliQ purification system), and EtOH with the following volume fractions: *b* ($\varphi_{BDA} = 0.433$; $\varphi_{H2O} = 0.032$; $\varphi_{EtOH} = 0.369$); *c* ($\varphi_{BDA} = 0.367$; $\varphi_{H2O} = 0.040$; $\varphi_{EtOH} = 0.387$); *d* ($\varphi_{BDA} = 0.303$; $\varphi_{H2O} = 0.051$; $\varphi_{EtOH} = 0.395$); *e* ($\varphi_{BDA} = 0.210$; $\varphi_{H2O} = 0.103$; $\varphi_{EtOH} = 0.385$). Hexadecyltrimethylammonium cations (CTA^+; Sigma Aldrich) were dissolved as 200 mM stock solution in EtOH and added to the mixtures *b* ($\varphi_{200\,mM\ CTA+} = 0.030$), *c* ($\varphi_{200\,mM\ CTA+} = 0.031$), *d* ($\varphi_{200\,mM\ CTA+} = 0.032$), and *e* ($\varphi_{200\,mM\ CTA+} = 0.075$) to obtain 15 mM CTA^+ in the bijel precursor. The concentrated Ludox TMA dispersion was added to precursor *b* ($\varphi_{Ludox\ TMA} = 0.136$), *c* ($\varphi_{Ludox\ TMA} = 0.175$), *d* ($\varphi_{Ludox\ TMA} = 0.219$), and *e* ($\varphi_{Ludox\ TMA} = 0.227$) yielding a particle concentration of 11 wt.% in the precursor mixture. The photo-initiator 2-hydroxy-2-methylpropiophenone (Sigma Aldrich) was incorporated to 3–5 wt.% to the bijel precursor to polymerize the BDA monomers after phase separation. A detailed overview of the sample preparation including precursor *a* ($\varphi_{BDA} = 0.500$; $\varphi_{H2O} = 0.140$; $\varphi_{EtOH} = 0.360$) was provided in Section S3 (Supporting Information). Visualization of the BDA-rich phase was accomplished by fluorescent labeling with Nile red (Sigma Aldrich). All chemicals were purchased as analytical grade.

Roll-to-Roll Bijel Film Fabrication: The bijel precursor had pumped at a rate of 2–4 mL min^{-1} through a rectangular slit of 0.5–1.5 mm width and 100 µm height onto polyethylene terephthalate foil (PET; 100 µm thickness; Reflectiv). The slit was built from three microscopy coverslips (20 × 20 × 0.1 mm; Menzel-Gläser) as shown in detail in Section S1 (Supporting Information). All inner glass surfaces of the slit were coated with a solution of 0.2 wt.% poly(diallyldimethylammonium chloride) (PDADMAC; Sigma Aldrich) and 500 mM NaCl (Merck) to prevent adhesion of the precursor mixture. After positioning the coating slit at an angle of ≈55° above the PET substrate, the PET was pulled at a default speed of 5 cm s^{-1} through the R2R setup by means of an electric motor (E192 Geared DC Motor; Mclennan Servo Supplies) with power regulator (DC Motor Speed Controller, PWM DC 6–60 V; Aidepen). The R2R-setup was submerged in a container of 1–2 m length filled with demineralized water (MilliQ purification system) which was brought to pH 3 by the addition of 1 M HCl. UV-polymerization of the membrane was accomplished by exposure to a high-intensity UV-lamp (OmniCure Series 1500).

The rollers to guide the substrate through the R2R machine were 3D-printed with a polylactic acid filament of 4 cm width and 2.5 cm diameter (Monoprice 3D printer filament; Dremel DigiLab). All holders for rollers, substrate stock rolls, and film collection were built with Lego bricks (for details see Section S2, Supporting Information).

Contact Angle Measurements: Particle-free precursor mixtures of liquid composition *a–d* were prepared containing 50 mM CTA^+. For all mixtures, the nanoparticle volume fraction $\varphi_{Ludox\ TMA}$ was replaced by water. 5 µL of each precursor mixture was deposited on PET substrate in a glass cylinder filled with water of pH 3 (setup shown in Section S4, Supporting Information). The droplet behavior was observed and recorded from the side view with a camera (25 fps; Thorlabs CS165MU/M). All images were analyzed with the software Fiji ImageJ (version 1.53k14). The dynamical apparent contact angle was averaged from five side-view images by ellipsoid fitting.

Interfacial Tension Measurement: The interfacial tensions $\gamma_{PM/H2O}$ of the precursor mixtures with liquid compositions *a–d* in water were estimated from drop shape analysis employing a pendant drop tensiometer (Dataphysics OCA25). Precursor mixtures without CTA^+ and Ludox TMA nanoparticles were injected at 8 µL s^{-1} into water and videos of the droplet formation were recorded at 42 fps. The interfacial tension was analyzed from the shape of the precursor droplet based on the Young-Laplace equation (ImageJ; version 1.53k14; plugin "pendant drop"[46]) before the droplet pinches off from the dispensing needle (Figure S6, Supporting Information).

Bijel Film Structure Characterization: Bijel films were analyzed by confocal laser scanning microscopy (Stellaris 5, Leica Microsystems). After polymerization, the bijel film was washed in a solution of 50 vol% 1 M HCl and 50 vol% ethanol to remove CTA^+. The film was then immersed in an alkaline Rhodamine 110 (Chemodex) solution and made optically transparent by replacing water with diethyl phthalate (Acros Organics). Upon excitement with 488 nm laser light, the Rhodamine 110 labeled

particles emit green fluorescence which was detected at 500–550 nm. The Nile red fluorescence of the polyBDA was excited with 561 nm laser light and detected at 600–700 nm (see Section S6, Supporting Information). The film cross-section was imaged via scanning electron microscopy (Phenom ProX, Thermo Fisher Scientific) by applying an electron beam excitation of 10 kV and an 8 nm layer of sputter-coated platinum.

Supporting Information

Supporting Information is available from the Wiley Online Library or from the author.

Acknowledgements

H.S. and M.R. contributed equally to this work. This publication is part of the project "Bijel templated membranes for molecular separations" (with project number 18632 of the research program Vidi 2019) which is financed by the Dutch Research Council (NWO).

Conflict of Interest

The authors declare no conflict of interest.

Data Availability Statement

The data that support the findings of this study are available from the corresponding author upon reasonable request.

Keywords

bijels, nanocomposites, nanoparticles, phase separation, Pickering emulsion, self-assembly, separation membranes

Received: October 18, 2023
Revised: November 27, 2023
Published online: December 18, 2023

[1] D. L. Gin, R. D. Noble, *Science* **2011**, *332*, 674.
[2] A. Pendse, S. Cetindag, M. H. Lin, A. Rackovic, R. Debbarma, S. Almassi, B. P. Chaplin, V. Berry, J. W. Shan, S. Kim, *Small* **2019**, *15*, 1904590.
[3] Y. Zhu, W. Xie, S. Gao, F. Zhang, W. Zhang, Z. Liu, J. Jin, *Small* **2016**, *12*, 5034.
[4] G. R. Guillen, Y. Pan, M. Li, E. M. V. Hoek, *Ind. Eng. Chem. Res.* **2011**, *50*, 3798.
[5] M. F. Haase, K. J. Stebe, D. Lee, *Adv. Mater.* **2015**, *27*, 7065.
[6] D. M. Wang, A. Venault, J. Y. Lai, *Hollow Fiber Membranes*, Elsevier **2021**, 13.
[7] M. Cui, T. Emrick, T. P. Russell, *Science* **2013**, *342*, 460.
[8] M. A. Khan, A. J. Sprockel, K. A. Macmillan, M. T. Alting, S. P. Kharal, S. Boakye-Ansah, M. F. Haase, *Adv. Mater.* **2022**, *34*, 2109547.
[9] K. Stratford, R. Adhikari, I. Pagonabarraga, J.-C. Desplat, M. E. Cates, *Science* **2005**, *309*, 2198.
[10] E. M. Herzig, K. A. White, A. B. Schofield, W. C. K. Poon, P. S. Clegg, *Nat. Mater.* **2007**, *6*, 966.
[11] M. N. Lee, A. Mohraz, A. Mohraz, *Adv. Mater.* **2010**, *22*, 4836.
[12] D. J. French, A. B. Schofield, J. H. J. Thijssen, *Adv. Mater. Interfaces* **2022**, *9*, 2102307.
[13] M. F. Haase, H. Jeon, N. Hough, J. H. Kim, K. J. Stebe, D. Lee, *Nat. Commun.* **2017**, *8*, 1.
[14] H. Siegel, A. J. Sprockel, M. S. Schwenger, J. M. Steenhoff, I. Achterhuis, W. M. De Vos, M. F. Haase, *ACS Appl. Mater. Interfaces* **2022**, *14*, 43195.
[15] T. Park, G. H. Choi, D. Lee, P. J. Yoo, *J. Memb. Sci.* **2021**, *634*, 119386.
[16] S. Boakye-Ansah, M. S. Schwenger, M. F. Haase, *Soft Matter* **2019**, *15*, 3379.
[17] S. P. Kharal, R. P. Hesketh, M. F. Haase, *Adv. Funct. Mater.* **2020**, *30*, 2003555.
[18] T. Wang, R. A. Riggleman, D. Lee, K. J. Stebe, *Mater. Horiz.* **2023**, *10*, 1385.
[19] A. J. Sprockel, M. A. Khan, M. De Ruiter, M. T. Alting, K. A. Macmillan, M. F. Haase, *Coll. Surfaces Physicochem. Eng. Asp.* **2023**, *666*, 131306.
[20] S. P. Kharal, M. F. Haase, *Small* **2022**, *18*, 2106826.
[21] C. Huang, J. Forth, W. Wang, K. Hong, G. S. Smith, B. A. Helms, T. P. Russell, *Nat. Nanotechnol.* **2017**, *12*, 1060.
[22] T. Wang, G. Di Vitantonio, K. J. Stebe, D. Lee, *ACS Mater Lett* **2020**, *2*, 524.
[23] J. Li, M. Wang, *Langmuir* **2023**, *39*, 1434.
[24] J. Li, H. Sun, M. Wang, *Langmuir* **2020**, *36*, 14644.
[25] X. Dong, T. J. Jeong, E. Kline, L. Banks, E. Grulke, T. Harris, I. C. Escobar, T. Harris, *J. Memb. Sci.* **2020**, *614*, 118510.
[26] M. Pagliero, A. Bottino, A. Comite, C. Costa, **2020**, *J. Memb. Sci. 596*, 117575.
[27] H. H. Wang, J. T. Jung, J. F. Kim, S. Kim, E. Drioli, Y. M. Lee, *J. Memb. Sci.* **2019**, *574*, 44.
[28] R. Søndergaard, M. Hösel, D. Angmo, T. T. Larsen-Olsen, F. C. Krebs, *Mater. Today* **2012**, *15*, 36.
[29] K. Hwang, Y. S. Jung, Y. J. Heo, F. H. Scholes, S. E. Watkins, J. Subbiah, D. J. Jones, D. Y. Kim, D. Vak, *Adv. Mater.* **2015**, *27*, 1241.
[30] S. Bae, H. Kim, Y. Lee, X. Xu, J.-S. Park, Y. Zheng, J. Balakrishnan, T. Lei, H. Ri Kim, Y. I. Song, Y.-J. Kim, K. S. Kim, B. Özyilmaz, J.-H. Ahn, B. H. Hong, S. Iijima, *Nat. Nanotechnol.* **2010**, *5*, 574.
[31] M. Bariya, Z. Shahpar, H. Park, J. Sun, Y. Jung, W. Gao, H. Y. Y. Nyein, T. S. Liaw, L.-C. Tai, Q. P. Ngo, M. Chao, Y. Zhao, M. Hettick, G. Cho, A. Javey, **2018**, *ACS Nano. 12*, 6978.
[32] H. Li, H. Liu, C. Shi, J. Qin, Y. Fu, Y. Song, Y. Li, Z. Ling, Z. Ling, *Adv. Mater. Interfaces* **2023**, *10*, 2300301.
[33] B. P. Binks, J. A. Rodrigues, W. J. Frith, *Langmuir* **2007**, *23*, 3626.
[34] D. Cai, P. S. Clegg, T. Li, K. A. Rumble, J. W. Tavacoli, *Soft Matter* **2017**, *13*, 4824.
[35] M. Lundgren, N. L. Allan, T. Cosgrove, N. George, *Langmuir* **2002**, *18*, 10462.
[36] M. Reeves, K. Stratford, J. H. J. Thijssen, *Soft Matter* **2016**, *12*, 4082.
[37] S. Boakye-Ansah, M. A. Khan, M. F. Haase, *J. Phys. Chem. C* **2020**, *124*, 12417.
[38] B. P. Binks, J. A. Rodrigues, *Angew. Chemie. Int. Ed.* **2007**, *46*, 5389.
[39] B. P. Binks, *Curr. Opin. Colloid Interface Sci.* **2002**, *7*, 21.
[40] M. F. Haase, J. Brujic, **2014**, *Angew. Chemie. Int. Ed. 53*, 11793.
[41] J. A. Witt, D. R. Mumm, A. Mohraz, **2016**, *J. Mater. Chem. A 4*, 1000.
[42] D. Cai, F. H. Richter, J. H. J. Thijssen, P. G. Bruce, P. S. Clegg, *Mater. Horizons* **2018**, *5*, 499.
[43] S. J. Gross, M.-T. Hsieh, D. R. Mumm, L. Valdevit, A. Mohraz, *Extrem. Mech. Lett.* **2022**, *54*, 101746.
[44] K. M. Mcdevitt, D. R. Mumm, A. Mohraz, *ACS Appl. Energy Mater.* **2019**, *2*, 8107.
[45] T. J. Thorson, E. L. Botvinick, A. Mohraz, *ACS Biomater. Sci. Eng.* **2018**, *4*, 587.
[46] A. Daerr, A. Mogne, *J. Open Res. Softw.* **2016**, *4*, 3.